

Primordial black holes with a massless scalar field

Tomohiro Harada* and B. J. Carr†

*Astronomy Unit, School of Mathematical Sciences, Queen Mary,
University of London, Mile End Road, London E1 4NS, UK*

(Dated: December 2, 2024)

The evolution of primordial black holes in a flat Friedmann universe with a massless scalar field is investigated in fully general relativistic numerical relativity. It is found that a primordial black hole is formed with a scale comparable to the cosmological horizon and may go through an initial phase with significant accretion. However, it soon gets smaller than the cosmological horizon and thereafter it can be approximated as an isolated vacuum solution with decaying mass accretion. In this situation the dynamical and inhomogeneous scalar field is typically equivalent to a perfect fluid with a stiff equation of state $p = \rho$. It is found that the gravitational memory scenario, proposed for primordial black holes in Brans-Dicke and scalar-tensor theories of gravity, is highly unphysical.

PACS numbers: 04.70.Bw, 97.60.Lf, 04.25.Dm, 95.35.+d

I. INTRODUCTION

The observed anisotropy and polarisation of the cosmic microwave background radiation give very precise information about the cosmic history since last scattering. Using a simple physical model, we can determine cosmological parameters with very high accuracy and also learn about structure formation and reionisation. Nevertheless, it is still difficult to obtain information about the universe before big bang nucleosynthesis without making many extra assumptions. In this context, primordial black holes (PBHs) could be one of the most important fossils of the very early universe. Such black holes may have formed directly from primordial density perturbations [1] and may contribute to the cosmological γ -ray background radiation, the cosmic ray flux and the dark matter density. This leads to important observational constraints on the number of PBHs [2] and hence on models of the very early universe.

To understand these constraints, it is important to know whether PBHs can accrete enough to become much more massive than they were at formation. In this context, the study of spherically symmetric self-similar solutions containing PBHs in a Friedmann background has proved very useful. Solutions of this kind containing a perfect fluid have been studied by several authors [3, 4, 5, 6], with particular emphasis on the radiation ($p = \rho/3$) and stiff fluid ($p = \rho$) cases. See [7] for a review of self-similar solutions. The conclusion is that there are no self-similar PBH solutions if the black hole is formed by purely local processes (i.e. if the background is exactly Friedmann beyond some radius); self-similar solutions are possible only if the initial perturbation of the Friedmann background extends to infinity. If the formation and evolution of a PBH in a general fluid universe with a local perturbation is simulated numerically, without assuming self-similarity, it is found that the PBH soon becomes much smaller than the cosmological horizon and this excludes self-similar growth [8, 9]. More recently, the threshold for PBH formation from density perturbations has been investigated in the context of critical phenomena [10, 11, 12, 13].

Hitherto studies of PBHs have mainly focused on perfect fluid universes with equation of state $p = k\rho$. However, it is also natural to consider a universe whose density is dominated by a scalar field. For example, in the chaotic inflation scenario, it is postulated that there is a pre-inflationary stage in which the scalar field moves randomly in space and time. In the pre-heating inflationary scenario, it is also natural to consider a scalar-field-dominated era [14]. The study of PBHs in the quintessence scenario has also attracted attention [15, 16].

Scalar fields are also relevant in Brans-Dicke and scalar-tensor theories of gravity, where the gravitational “constant” varies in space and time. This is because, if there is a single gravitational scalar field, such theories can be transformed into the usual Einstein gravity with a single scalar field [17]. Brans-Dicke and scalar-tensor theories are particularly relevant to PBHs since the black holes may form when G was very different from today. Indeed the “gravitational memory” scenario has been proposed [18], in which the value of G within the black hole is assumed to be preserved as the cosmological background value evolves. The observational constraints on PBHs depend strongly on whether or not one has gravitational memory [19]. It is not clear whether this applies but, if it does, it should be due to the properties of the black hole event horizon rather than those of the matter fields involved. In fact, evidence against the gravitational memory scenario has been obtained for special cases [20, 21].

* Electronic address:T.Harada@qmul.ac.uk

† Electronic address:B.J.Carr@qmul.ac.uk

In this paper, as a first step to investigating these questions, we consider a universe containing a massless scalar field but no matter. To implement numerical simulations, we use a double-null formulation of the Einstein equations based on the work by Hamadé and Stewart [22]. This has been shown to be a very powerful tool for investigating critical collapse [22] and the internal structure of black holes [23]. This is an improvement on earlier work [21], in which the gravitational effect of the scalar field was neglected, since it uses the full field equations. This paper should be seen in conjunction with two other papers [24, 25]. We adopt units in which $G = c = 1$ and the abstract index notation of [26].

II. DOUBLE-NULL FORMULATION OF THE EINSTEIN EQUATIONS

We consider a massless scalar field in general relativity, for which the stress-energy tensor is

$$T_{ab} = \Psi_{,a}\Psi_{,b} - \frac{1}{2}g_{ab}\Psi^{,c}\Psi_{,c}. \quad (2.1)$$

The Einstein equations are

$$R_{ab} - \frac{1}{2}g_{ab}R = 8\pi T_{ab}, \quad (2.2)$$

and the equation of motion for the scalar field is

$$\square\Psi = \Psi^{,a}_{,a} = 0. \quad (2.3)$$

We also focus on a spherically symmetric system, for which the line element can be written in the form

$$ds^2 = -A(u, v)dudv + r^2(u, v)(d\theta^2 + \sin^2\theta d\phi^2), \quad (2.4)$$

where u and v are advanced and retarded time coordinates, respectively, and r is the “area radius” (the proper area of the sphere of constant r being $4\pi r^2$). Eqs. (2.2) and (2.3) then imply that we have 14 first-order partial differential equations and two auxiliary equations (see Appendix A). By adopting an appropriate coordinate choice, we can simulate regions outside the cosmological horizon and inside the black hole horizon simultaneously (see Appendix B).

In spherically symmetric spacetimes the existence and position of apparent horizons can be inferred from the form of the Hawking mass. This is a well-behaved quasi-local mass, which can be written as

$$m = \frac{r}{2} \left(1 + \frac{4r_{,u}r_{,v}}{A} \right). \quad (2.5)$$

Using Eq. (2.5) and the equations in Appendix A, we can derive the following useful relations:

$$m_{,u} = -\frac{8\pi r^2 r_{,v}(\Psi_{,u})^2}{A}, \quad (2.6)$$

$$m_{,v} = -\frac{8\pi r^2 r_{,u}(\Psi_{,v})^2}{A}. \quad (2.7)$$

A region where $r_{,u} < 0$ and $r_{,v} < 0$ is trapped, while one where $r_{,u} > 0$ and $r_{,v} > 0$ is anti-trapped. The black hole and cosmological apparent horizons are defined as outer marginally trapped and anti-trapped surfaces, respectively. Providing the black hole horizon is within the cosmological horizon, these correspond to the conditions $r_{,u} = 0$ and $r_{,v} = 0$, respectively. Thus the relation $r = 2m$ is satisfied on both apparent horizons because $r_{,u}r_{,v} = 0$ there. We confine attention to this situation in the present paper. However, as discussed in a separate paper [25], in some circumstances the black hole horizon can be outside the cosmological horizon and the situation is then more complicated. In this case, we can still define the outer and inner apparent horizons, $\text{AH}(\text{out})$ and $\text{AH}(\text{in})$, as the surfaces on which $r_{,v} = 0$ and $r_{,u} = 0$, respectively. However, these are no longer everywhere identified with the black hole and cosmological apparent horizons.

We first consider the flat Friedmann model, for which $A(u, v)$, $r(u, v)$ and $m(u, v)$ are given explicitly in terms of the standard double null coordinates in Appendix B. The condition $2m = r$ implies that the cosmological apparent horizon is $3u + v = 0$. On the other hand, the cosmological particle horizon is clearly $u = 0$, corresponding to a photon propagating outwards from the big bang. This shows that the apparent horizon is always outside the particle horizon and the conformal diagram of the spacetime is as indicated in Fig. 1. This also shows the initial (big bang) spacelike singularity. If one perturbs such a spacetime but without introducing a black hole, the conformal diagram remains

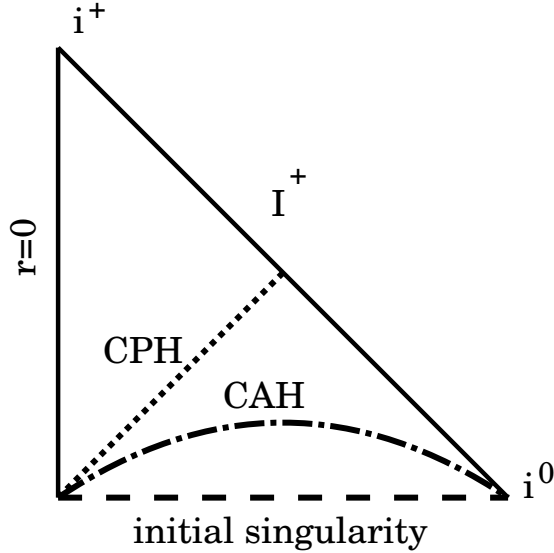


FIG. 1: The conformal diagram of the flat Friedmann spacetime with a massless scalar field. The cosmological apparent horizon is spacelike and outside the cosmological particle horizon.

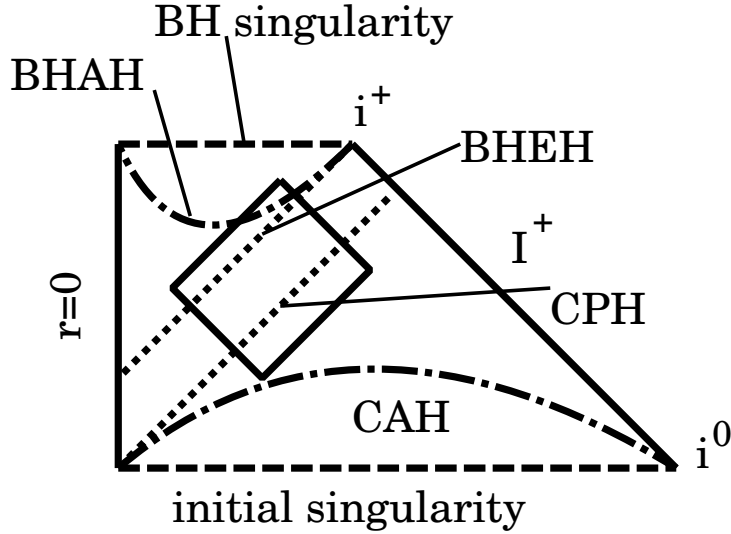


FIG. 2: The conformal diagram of the possible causal structure of the calculated model. The region enclosed by a diamond is the calculated region $[u_0, u_1] \times [v_0, v_1]$.

the same but the trajectories of constant space and time coordinate change. If one has a black hole embedded in an exact or asymptotically flat Friedmann model, the conformal diagram will change to the form indicated in Fig. 2. There is now also a black hole event horizon and apparent horizon, although one cannot give explicit expressions for these, and a final (black hole) spacelike singularity.

If we define time and space coordinates, T and X , by

$$u = T - X, \quad (2.8)$$

$$v = T + X, \quad (2.9)$$

we can put the 2-dimensional part of the metric tensor into conformally flat form. As in the usual 3+1 approach, we can define the energy density ρ_H and momentum density J measured by an observer moving normal to the $T = \text{const}$ spacelike hypersurface by

$$\rho_H \equiv T_{ab} \hat{T}^a \hat{T}^b, \quad (2.10)$$

$$J \equiv -T_{ab}\hat{T}^a\hat{X}^b, \quad (2.11)$$

where \hat{T}^a and \hat{X}^b are unit vectors parallel to T^a and X^b , respectively.

It should be stressed that the above description is observer-dependent and one can adopt another point of view. Providing the scalar field is vorticity-free and has a timelike gradient, it is equivalent to a perfect fluid with a “stiff” equation of state $p = \rho$ [27]. The stress-energy tensor is then

$$T^{ab} = \rho_S(g^{ab} + 2U^aU^b), \quad (2.12)$$

where the energy density ρ_S and the 4-velocity U^a of the stiff fluid are

$$\rho_S = -\frac{1}{2}\Psi_{,a}\Psi^{,a}, \quad (2.13)$$

$$U_a = \frac{-\Psi_{,a}}{\sqrt{-\Psi^{,b}\Psi_{,b}}}. \quad (2.14)$$

It should be noted that the 4-velocity of the stiff fluid is parallel to the timelike gradient of the scalar field. We can define an observer-independent velocity function by

$$V \equiv \frac{dr}{d\tau} = r_{,a}U^a, \quad (2.15)$$

this being the rate of increase of r per unit proper time τ along the worldline of the equivalent stiff fluid element. Appendix A gives expressions for these physical quantities in terms of the quantities calculated numerically.

III. INITIAL DATA FOR PBHS

A. Structure of initial data

The initial data are prescribed on the outgoing null surface $u = u_0$ and the ingoing null surface $v = v_0$. The region of calculation is the diamond $[u_0, u_1] \times [v_0, v_1]$ shown in Fig. 3, which is also equivalent to the diamond in Fig. 2. We have three independent functions on the two null surfaces: A , Ψ and r . Two of them can be chosen freely and the other one is determined by the initial value equations on the null surfaces. It is convenient to choose

$$A(u_0, v), A(u, v_0), \Psi(u_0, v), \Psi(u, v_0) \quad (3.1)$$

as the free initial data and to regard

$$r(u_0, v), r(u, v_0) \quad (3.2)$$

as being determined by the initial value equations. We can regard $\Psi(u_0, v)$ and $\Psi(u, v_0)$ as the physical degrees of freedom in the initial data, while the choice for $A(u_0, v)$ and $A(u, v_0)$ fixes the gauge.

B. Upper limit on the black hole radius

It is usually assumed that the perturbation from which the PBH forms is local. Since information propagates at the speed of light, the matching between the perturbed and flat Friedmann regions always corresponds to some outgoing null ray $u = u_m = \text{const}$. This means that the region outside the matching null surface $u = u_m$ is always described by the flat Friedmann solution. On the outgoing null surface $u = u_0$, we therefore assume that the initial data are given by the flat Friedmann solution for $v_0 \leq v \leq v_1$. On the ingoing null surface $v = v_0$, we assume they are given by the flat Friedmann solution for $u_0 \leq u < u_m$ but by some perturbation of it for $u_m \leq u \leq u_1$, where an appropriate matching is implemented at $u = u_m$.

When the initial perturbation is given locally and causally propagated thereafter, the matching should be implemented within the cosmological particle horizon, i.e. $u_m \geq u_{\text{CPH}}(v)$ on the ingoing null surface $v = \text{const}$. Here $u = u_{\text{CPH}}(v) = \text{const}$ denotes the location of the cosmological particle horizon in the flat Friedmann universe. Since $u_{\text{CPH}}(v) > u_{\text{CAH}}(v)$, we have $r(u_{\text{BAAH}}(v), v) \leq r(u_{\text{CPH}}(v), v)$ and $m(u_{\text{BAAH}}(v), v) \leq m(u_{\text{CPH}}(v), v)$ from Eq. (2.6).

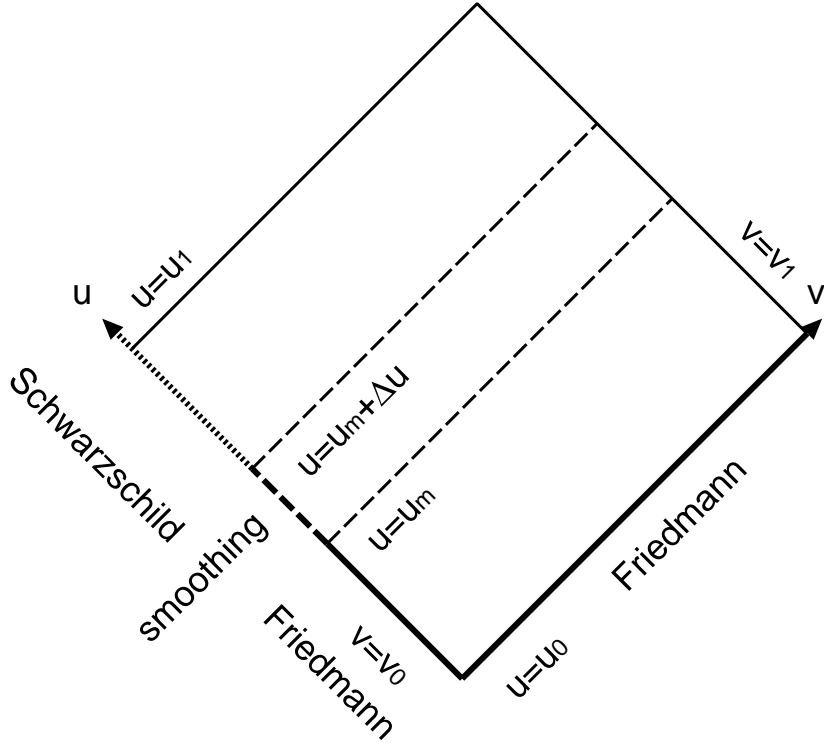


FIG. 3: Schematics figure of the initial data setting.

Hereafter we use the abbreviation $r_{\text{BAAH}}(v) = r(u_{\text{BAAH}}(v), v)$ etc. Since $r = 2m$ at the black hole apparent horizon and $r = 8m$ at the cosmological particle horizon (see Appendix B 1), we have

$$\frac{r_{\text{BAAH}}(v)}{r_{\text{CPH}}(v)} = \frac{r_{\text{BAAH}}(v)}{2m_{\text{BAAH}}(v)} \frac{m_{\text{BAAH}}(v)}{m_{\text{CPH}}(v)} \frac{2m_{\text{CPH}}(v)}{r_{\text{CPH}}(v)} \leq \frac{1}{4}. \quad (3.3)$$

The equality holds only when $\Psi = \text{const}$ on the ingoing null surface $v = \text{const}$ for $u \geq u_m$ and $u_m = u_{\text{CPH}}$. In other words, the black hole apparent horizon is much smaller than the cosmological particle horizon. This result is easily extended to a perfect fluid with the equation of state $p = k\rho$ ($1/3 < k \leq 1$) and more general matter fields. This is discussed elsewhere [24] with a more rigorous treatment. For the flat Friedmann solution with a massless scalar field, the trajectory of the cosmological apparent horizon is spacelike and outside the cosmological particle horizon (see Appendix B 1), so the ratio of the black hole and cosmological apparent horizon sizes is even less than $1/4$.

Despite the above causality constraints, it should be noted that a perturbation can be larger than the cosmological particle horizon in some circumstances, e.g. for quantum fluctuations resulting from inflation. In this case, the only upper limit on the size of the perturbation comes from the requirement that the perturbed region is part of our universe rather a separate closed universe. The condition for this has been derived precisely for the situation in which the collapsing region is homogeneous and the equation of state is $p = k\rho$ [24]. For this reason, some of the situations we simulate in this paper violate Eq. (3.3).

C. Setting up the initial data

In the flat Friedmann region, we choose the coordinate system given in Appendix B 1. We also impose flat Friedmann initial data for A and Ψ on the initial outgoing null surface $u = u_0$ with $v_0 \leq v \leq v_1$. This is given by Appendix B 1. On the initial ingoing null surface $v = v_0$, we choose flat Friedmann data for A for $u_0 \leq u \leq u_1$. For the function Ψ , we use the same data on the initial ingoing null surface for $u_0 \leq u \leq u_m$, but $\Psi = \text{const}$ for $u_m + \Delta u < u \leq u_1$. This is equivalent to Schwarzschild data in coordinates penetrating the black hole (cf. Appendix B 2). The sudden transition from flat Friedmann data to Schwarzschild data results in a discontinuity at $u = u_m$, which reduces the numerical accuracy. Hence we smooth the transition with some smoothing length Δu ; we use a quadratic function

between u_m and $u_m + \Delta u$, so that Ψ and $\Psi_{,u}$ are continuous. More precisely, we impose the following initial data:

$$A(u, v_0) = C^2 \left(\frac{u + v_0}{2} \right), \quad (3.4)$$

$$s(u, v_0) \equiv \sqrt{4\pi}\Psi = \begin{cases} \frac{\sqrt{3}}{2} \ln \left(\frac{u + v_0}{2} \right) + s_0, & \text{for } u < u_m \\ \frac{\sqrt{3}}{2} \left[\frac{(\Delta u)^2 - (u_m + \Delta u - u)^2}{2\Delta u(u_m + \Delta u)} + \ln \left(\frac{u_m + v_0}{2} \right) \right] + s_0, & \text{for } u_m \leq u < u_m + \Delta u \\ \frac{\sqrt{3}}{2} \left[\frac{\Delta u}{2(u_m + v_0)} + \ln \left(\frac{u_m + v_0}{2} \right) \right] + s_0, & \text{for } u \geq u_m + \Delta u \end{cases}, \quad (3.5)$$

on the initial ingoing null surface $v = v_0$, and

$$A(u_0, v) = C^2 \left(\frac{u_0 + v}{2} \right), \quad (3.6)$$

$$s(u_0, v) = \frac{\sqrt{3}}{2} \ln \left(\frac{u_0 + v}{2} \right) + s_0, \quad (3.7)$$

on the initial outgoing null surface $u = u_0$. Here C and s_0 are constants and, without loss of generality, we can choose $C = 1$ and $s_0 = 0$. Note that although one has a Schwarzschild vacuum for $u \geq u_m + \Delta u$, this situation only applies instantaneously at $v = v_0$, since the inflowing matter will fill this up almost immediately.

To summarise, two parameters describe the initial conditions: the location of the matching surface and the smoothing length. The region outside the matching surface is the exact flat Friedmann solution, so the first parameter determines the mass of the perturbed region. The second parameter determines the mass of the black hole compared to the perturbed mass. A small smoothing length means a narrow boundary between the exterior Friedmann region and the interior vacuum region. In this case, the mass inside the vacuum region is nearly the same as that at the matching surface and so a large mass is concentrated at the central singularity. A large smoothing length means a wide boundary, so the mass inside the vacuum region is much smaller than this and so a small mass is concentrated at the central singularity. For vanishing smoothing length, the black hole mass is the same as that at the matching surface, although it is difficult to implement this numerically because of the strong discontinuity.

IV. RESULTS

The numerical code is based on Hamadé and Stewart [22], which is described in detail in Appendix C. As indicated in Fig. 3, the calculated region is the diamond contained by u_0 , v_0 , u_1 and v_1 . The initial data are prescribed on the ingoing null surface $v_0 = 1$ and the outgoing null surface $u_0 = -0.5$. The values u_0 and v_0 fix the units. For example, the background value for the Hubble parameter at (u_0, v_0) is 4 and the Hubble length becomes 0.25 from Eq. (B8). The value of u_1 is always taken to be 1.1 but v_1 varies between 2 and 4. On the initial ingoing null surface, we make the matching at three values of u_m in the range -0.5 to 0 . We also use small and large smoothing lengths, corresponding to $\Delta u = 0.02$ and $\Delta u = 0.5$, respectively.

The cosmological apparent and particle horizons are given by $u_{\text{CAH}} = -v/3$ and $u_{\text{CPH}} = 0$, respectively (see Appendix B 1). As time proceeds, the outgoing null rays will become ever more sensitive to r near the black hole event horizon, so the calculation is stopped at $v = v_1$, when the outgoing null rays near the black hole event horizon become too coarse to resolve. Note that the radius of the unperturbed cosmological apparent horizon and the mass within it are given by

$$m_{\text{CAH}} = r_{\text{CAH}}/2 = Cv^{3/2}/(3\sqrt{3}) \quad (4.1)$$

(see Appendix B 1). Figure 2 shows the conformal diagram of the overall spacetime schematically. The model parameters and initial black hole to cosmological mass ratios are summarised in Table I.

We present results for four models. For Model A, a sharp matching is made at the cosmological apparent horizon. For Model B, a sharp matching is made at the cosmological particle horizon, which is well inside the cosmological apparent horizon. For Model C, a smooth matching is made at the cosmological apparent horizon. For Model D, a smooth matching is made well outside the cosmological apparent horizon, although the black hole itself is inside it. In a separate paper [25], we consider models in which a sharp matching is made well outside the cosmological apparent horizon but within the radius corresponding to a separate closed universe. These models have very different qualitative features, even the conformal diagram being modified, which is why we consider them separately. Note that the models are not causal except Model B, so that the ratio of the black hole size to the cosmological particle horizon size exceeds the limit of $1/4$ derived in Section II B.

TABLE I: Model parameters and initial mass within black hole event horizon compared to cosmological apparent horizon

Models	u_m	Δu	u_0	u_1	v_0	v_1	$m_{\text{BHEH}}/m_{\text{CAH}}$
A	-1/3	0.02	-0.5	1.1	1	4	0.972
B	0	0.02	-0.5	1.1	1	2	0.223
C	-1/3	0.5	-0.5	1.1	1	2.5	0.399
D	-0.5	0.5	-0.5	1.1	1	3.5	0.727

A. Black hole horizons

Figure 4 shows the locations of the black hole event horizon and apparent horizon and the cosmological apparent horizon in the (u, v) plane for the four models. In all cases, it is seen that the black hole apparent horizon is initially well within the event horizon but approaches it as time proceeds. In Fig. 4(b), the location of the (unperturbed) cosmological particle horizon of the exact flat Friedmann solution is also plotted. In other cases, the cosmological particle horizon of the exact flat Friedmann solution is also perturbed so that we do not plot it.

The radii and masses of the black hole apparent horizon and event horizon for Models A–D are shown, together with those for the cosmological horizons, in Figs. 5 and 6. The initial and final values and their ratios are also summarised in Tables II and III. The black hole apparent horizon, event horizon and the cosmological apparent horizon approximately coincide with each other at $v = 1$ for Model A, both in radius and mass, as seen in Figs. 5(a) and 6(a). Figs. 5 and 6 show that the qualitative features of the evolution for Models A–D are very similar. The radius of the cosmological apparent horizon of the unperturbed flat Friedmann solution grows like $v^{3/2}$, while the black hole apparent horizon and event horizon converge and grow much more slowly. As a consequence, the black hole horizons soon get much smaller than the cosmological apparent horizon. This is also the case for the corresponding masses.

TABLE II: Initial and final radii of black hole horizons and their ratios

Models	BHAH $v = v_0$	BHAH $v = v_1$	Ratio	BHEH $v = v_0$	BHEH $v = v_1$	Ratio
A	0.373	0.668	1.79	0.377	0.694	1.84
B	0.0858	0.124	1.44	0.0985	0.125	1.27
C	0.154	0.232	1.51	0.173	0.241	1.39
D	0.279	0.470	1.68	0.300	0.485	1.62

TABLE III: Initial and final masses within black hole horizons and their ratios

Models	BHAH $v = v_0$	BHAH $v = v_1$	Ratio	BHEH $v = v_0$	BHEH $v = v_1$	Ratio
A	0.187	0.334	1.79	0.187	0.334	1.79
B	0.0429	0.0614	1.43	0.0429	0.0614	1.43
C	0.0769	0.116	1.51	0.0769	0.116	1.51
D	0.140	0.235	1.68	0.140	0.235	1.68

Since the black hole event horizon is given by the curve $u = u_{\text{BHEH}} = \text{const}$, Eq. (2.7) gives the mass accretion rate of the black hole. This also serves as a consistency check for numerical accuracy. The result for Models A–D is shown in Fig. 7, where both sides of Eq. (2.7) are plotted. We find that the curves are almost indistinguishable, which implies very good numerical accuracy. For Model A, the accretion rate starts very small, then increases, reaches a maximum of 0.0691 at $v \simeq 1.75$ and then decreases to a very small value. Recall that the units are such that the background Hubble parameter is 4 and the background Hubble length is 0.25 at u_0 and v_0 . For Models B and C, the accretion rate starts with its maximum value and then monotonically decreases. The features for Model D are similar to those for Model A. We conclude that accretion is suppressed even for a PBH as large as the cosmological apparent horizon. This is because Eq. (2.7) implies that the mass accretion rate is proportional to $(-r_{,u})$ and this vanishes at the cosmological apparent horizon. Thus, even if a PBH starts off as large as the cosmological apparent horizon, it soon gets considerably smaller than this. In any case, after a short period with large accretion, which continues only for about a Hubble time, the accretion soon becomes ineffective. As seen in Tables II and III, the mass increase is at most 84 % for our models.

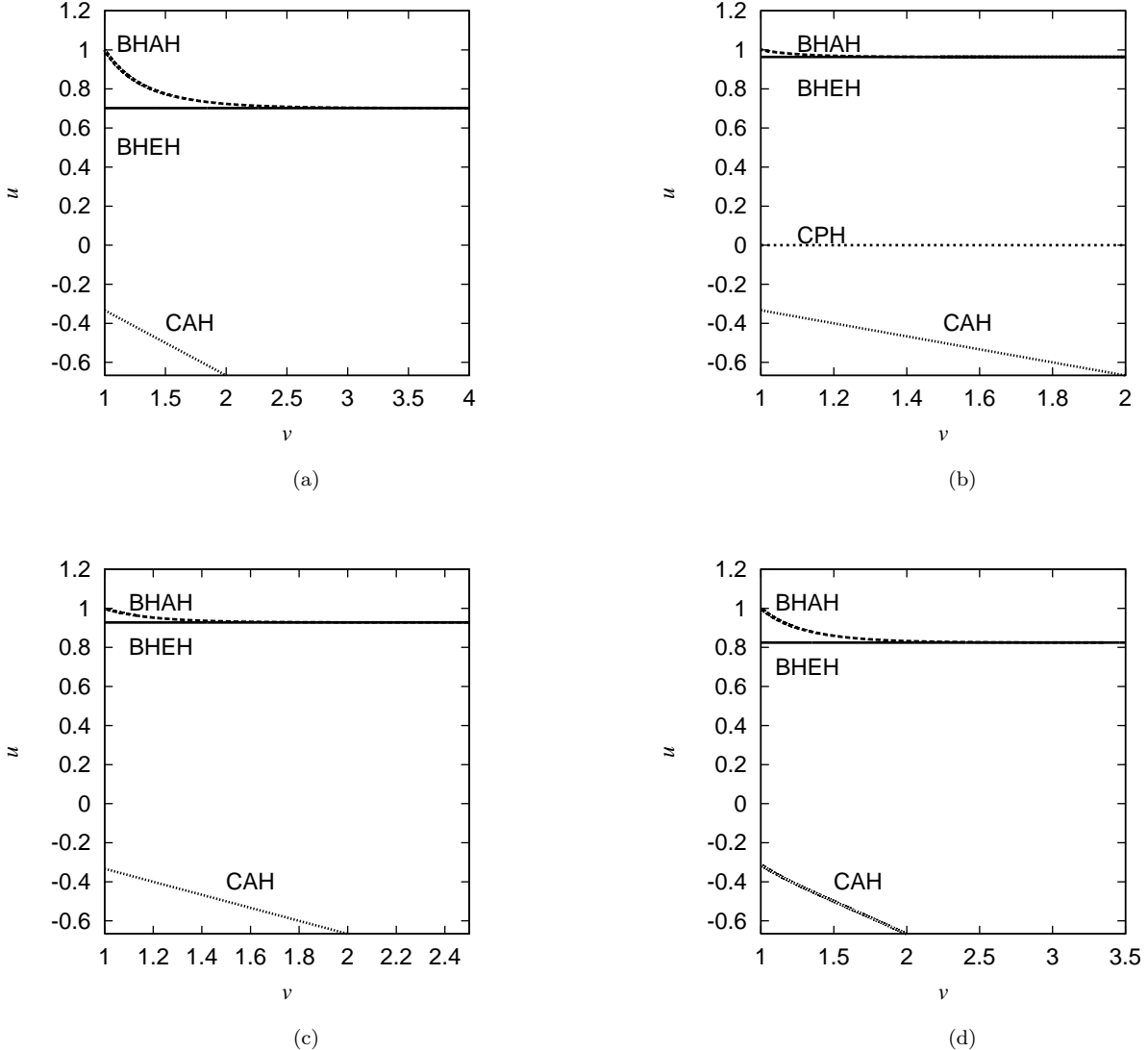


FIG. 4: The locations of the black hole event horizon, black hole apparent horizon, and cosmological apparent horizon in the (u, v) plane for Models A–D are plotted in (a)–(d), respectively. For Model B, the location of the cosmological particle horizon of the unperturbed flat Friedmann solution is also plotted.

B. Geometry and scalar field

Since the qualitative features of the numerical results are very similar for Models A–D, in this subsection we concentrate on Model A. Figure 8 shows the evolution of the area radius r in terms of u and v . We can see from Fig. 8(b) that there is a threshold value of u : outgoing null rays with smaller u go to infinity, while those with larger u go to the singularity at $r = 0$. Therefore, this threshold value can be identified with the black hole event horizon $u_{\text{BHEH}} \simeq 0.702$. Since $r_{,v}$ approaches zero along the black hole event horizon, all ingoing null rays seem to cross it at almost the same radius in Fig. 8(a). In fact, the integration is continued well beyond $v = v_1$ to locate the black hole event horizon accurately. Figure 8(b) shows that the radius of the black hole event horizon reaches 0.694 at $v = 4$.

Figure 9 shows the evolution of $2m/r$ in terms of u and v . There is an apparent horizon where this is unity. The signs of both ingoing and outgoing null expansions are the same when this is larger than unity. A region is untrapped when it is smaller than unity. As seen in Fig. 9(a), $2m/r$ is almost exactly unity in the perturbed region at the initial ingoing null surface $v = v_0 = 1$. As u increases, there then appears a black hole apparent horizon, beyond which the region is trapped. There is also a cosmological apparent horizon at $u = -1/3$ and $v = v_0 = 1$, although it goes outside

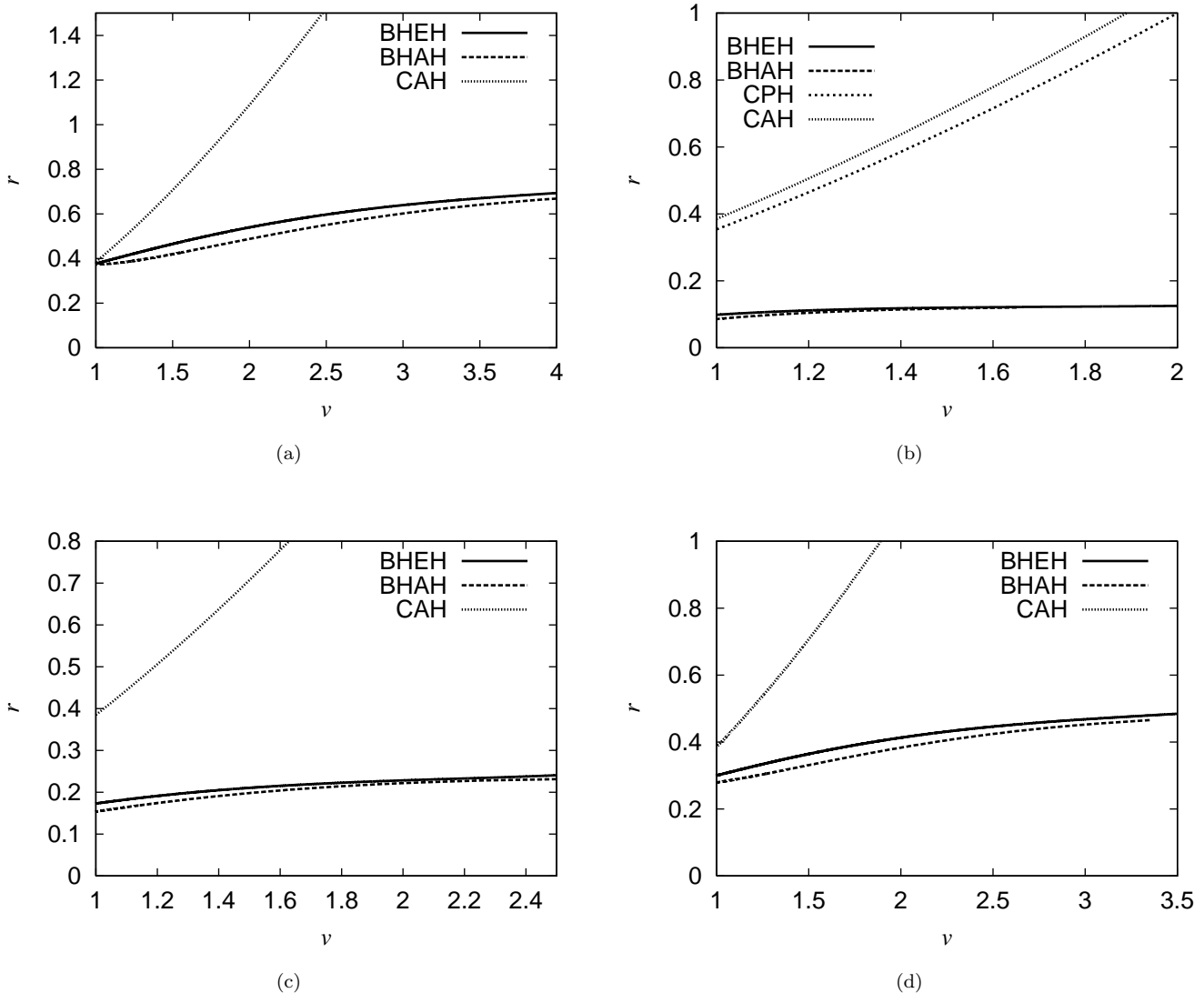


FIG. 5: The evolution of the area radius r of the black hole event horizon, black hole apparent horizon and cosmological apparent horizon for Models A–D is plotted in (a)–(d). For Model B, the radius of the cosmological particle horizon of the unperturbed flat Friedmann solution is also plotted.

the calculated region during the evolution. As time proceeds, the value of $2m/r$ in the untrapped region between the black hole and cosmological apparent horizons becomes smaller and the curve near the black hole apparent horizon becomes steeper. As seen in Fig. 9(b), there is no black hole apparent horizon before the event horizon forms at $u = u_{\text{BHEH}} \simeq 0.702$. At $u = u_{\text{BHEH}}$, $2m/r$ approaches unity from below as v increases. Soon after $u = u_{\text{BHEH}}$, a black hole apparent horizon appears.

Figure 10 shows the evolution of the scalar field for Model A. For clarity, it is plotted in terms of both (v, r) and (T, r) coordinates. In either case there is no coordinate singularity at the black hole horizons as the ingoing Eddington-Finkelstein coordinate is well-behaved for the Schwarzschild black hole. In the (v, r) diagram of Fig. 10(a), the solid and dashed curves give the results of the simulations and the evolution of the flat Friedmann solution, respectively. Because of the initial perturbation, the value of the scalar field in the perturbed region starts off much smaller than that of the flat Friedmann solution. Thereafter, the perturbed scalar field tends to evolve as in the flat Friedmann solution. Since the radius of the black hole event horizon is 0.694 at $v = 4$, the region inside the black hole event horizon is also calculated accurately. The evolution of the scalar field is well described by the flat Friedmann evolution with a small perturbation both outside and inside the black hole event horizon. The scalar field is smooth at the black hole event horizon. In the (T, r) diagram of Fig. 10(b), the heavy and light curves give the equivalent

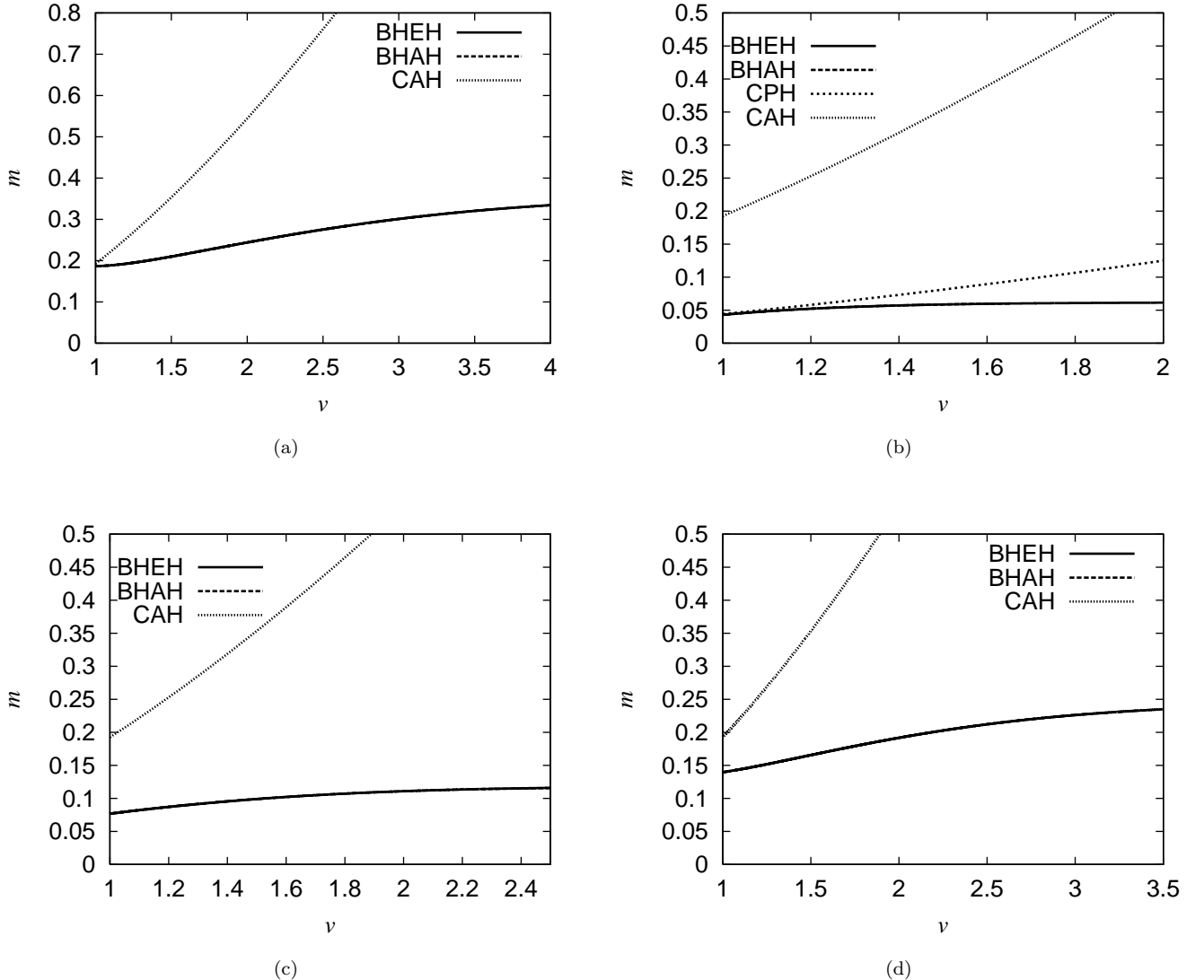


FIG. 6: The evolution of the mass m contained within the black hole event horizon, black hole apparent horizon and cosmological apparent horizon for Models A–D is plotted in (a)–(d). The curves for the black hole event horizon and the black hole apparent horizon are indistinguishable. For Model B, the mass contained within the cosmological particle horizon of the unperturbed flat Friedmann solution is also plotted.

results and the position of the event horizon is shown by the broken line. It should be stressed, however, that there is no unique choice of spatial hypersurface and the profile of Ψ would be different with a different choice.

Figure 11 shows the energy density ρ_H and momentum density J measured by the observer moving normal to the $T = \text{const}$ spacelike hypersurface for Model A. Since this normal observer coincides with the comoving observer in the flat Friedmann universe, J vanishes in the flat Friedmann region for $u < u_m$ (see Appendix B 1). In terms of the energy density ρ_H , there is an underdense region inside the flat Friedmann region. Inside this underdense region, there is an overdense region around the black hole event horizon, where the energy density increases with time. In terms of the momentum density J , there is considerable energy infall around the black hole event horizon. $|J|$ increases significantly near the black hole event horizon, although we should note that this is an observer-dependent view. [FIGURES SHOULD SHOW POSITION OF EVENT HORIZON]

Figure 12 shows the observer-independent quantities ρ_S and V . These are the energy density and velocity of the equivalent stiff fluid. The spikes correspond to the matching coordinate u_m . It is interesting that ρ_S is everywhere positive. This is a non-trivial result since ρ_S could in principle be negative if the spatial gradients were large enough. This is related to the fact, as illustrated in Fig. 12(a), that the gradient of the scalar field is always timelike in this

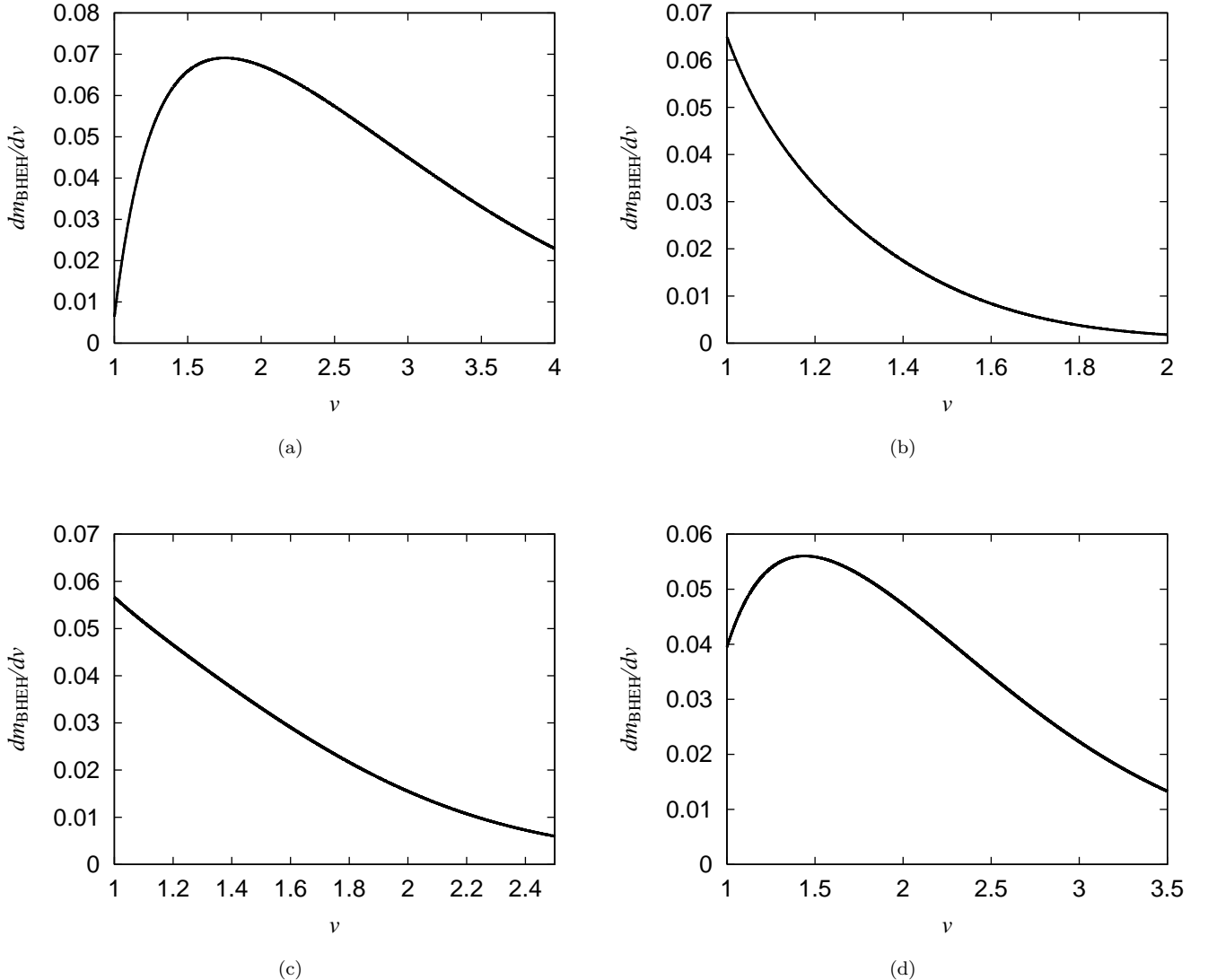


FIG. 7: The PBH mass accretion rate dm_{BHEH}/dv for Models A–D is plotted in (a)–(d). The solid and dashed lines denote the estimates of the left and right hand sides of Eq. (2.7), respectively, although these two lines are almost indistinguishable.

simulation. (Otherwise it would not be equivalent to a stiff fluid.) Also, in terms of the density ρ_S , we can see an underdense region just inside the flat Friedmann region. Within this underdense region, the energy density increases as one moves inwards. However, the energy density decreases nearly homogeneously for $v \geq 2.5$. In terms of the velocity V , the region near the black hole is infalling, as seen in Fig. 12(b), but the infall velocity profile near the black hole event horizon is almost stationary. We conclude that the growth of ρ_H and $|J|$ around the black hole event horizon is completely due to the Lorentz transformation. Physically, the energy density ρ_S is slowly decreasing and the infall velocity profile V is almost stationary near the black hole event horizon. These results suggest that the PBH can be regarded as almost isolated, with a relatively small mass accretion for $v \gtrsim 2$. This is consistent with the mass accretion rate seen in Fig. 7(a). Although there are seen apparent discontinuities at large radii in Figs. 11 and 12, this is only due to the narrow boundary and all quantities are continuous everywhere.

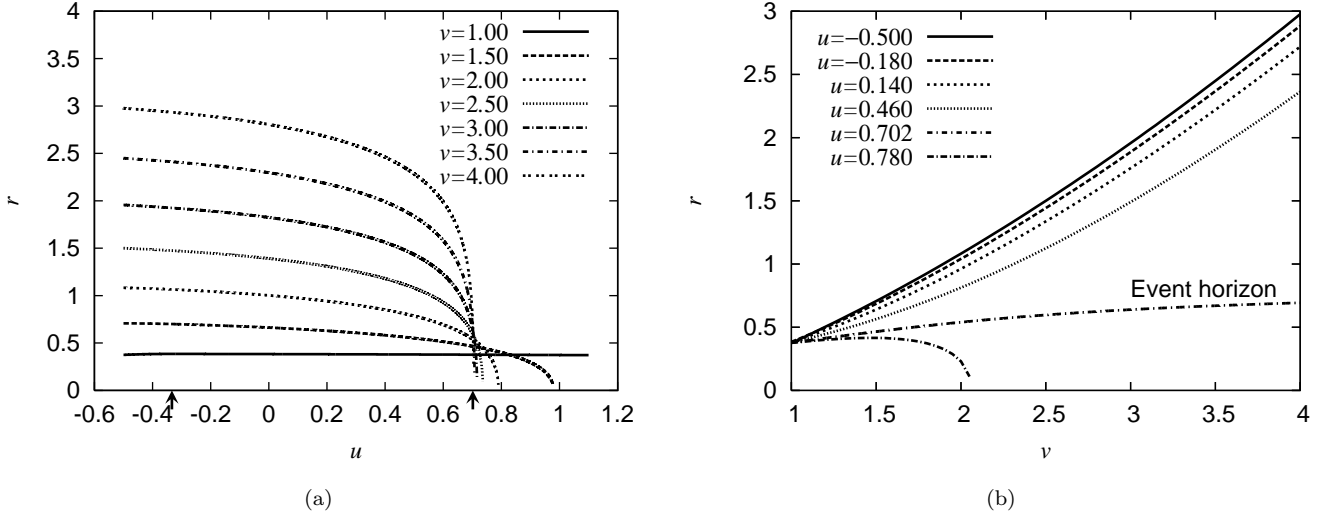


FIG. 8: The area radius r along (a) ingoing null rays $v = \text{const}$ and (b) outgoing null rays $u = \text{const}$ for Model A. The arrows at $u = u_m = -1/3$ and $u = u_{\text{BHEH}} \simeq 0.702$ in (a) denote the matching outgoing null surface and black hole event horizon, respectively.

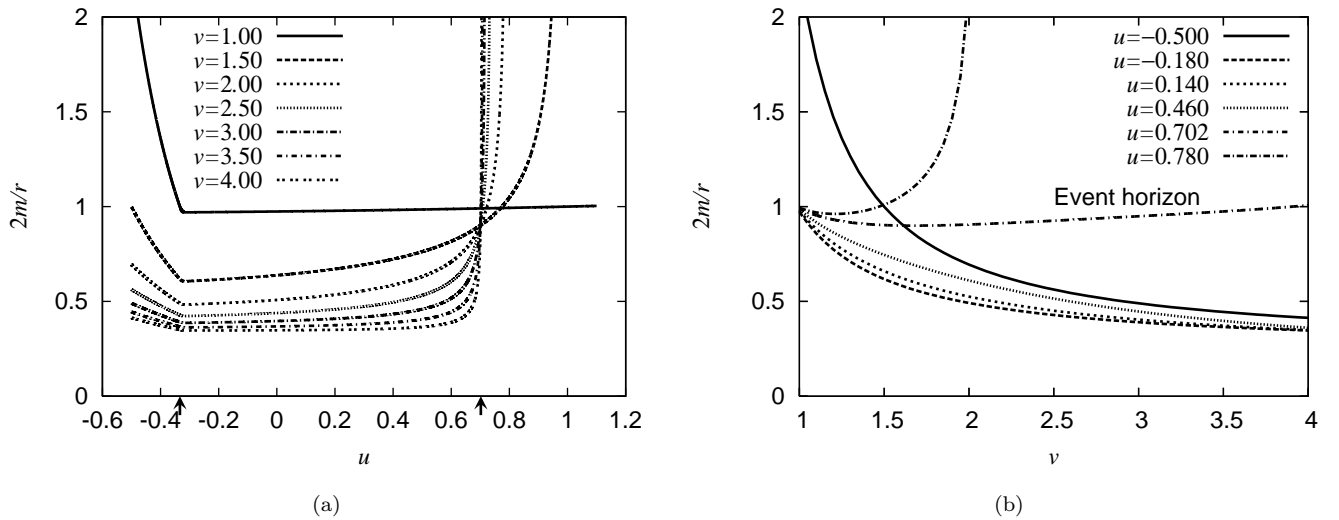


FIG. 9: Same as Fig. 8 but for $2m/r$.

V. DISCUSSION

A. Self-similar growth?

Since the cosmological time t is proportional to $(u + v)^{3/2}$ for the flat Friedmann solution (see Appendix B 1), the self-similar growth of a black hole would imply that its mass grows like $(u + v)^{3/2}$, as seen by a distant observer. It also implies that the black hole mass accretion rate dm_{BHEH}/dv would be proportional to $(u + v)^{1/2}$. However, the results of the present simulation show that the accretion rate will decrease after reaching a maximum. We conclude that there is no evidence for a trend towards self-similar evolution. In fact, it has been already shown analytically that there is no self-similar solution which contains a black hole attached to an exact flat Friedmann exterior solution [3, 4, 5, 6]. Note that this contradicts the argument [15] that a black hole can grow as fast as the Universe through accreting a

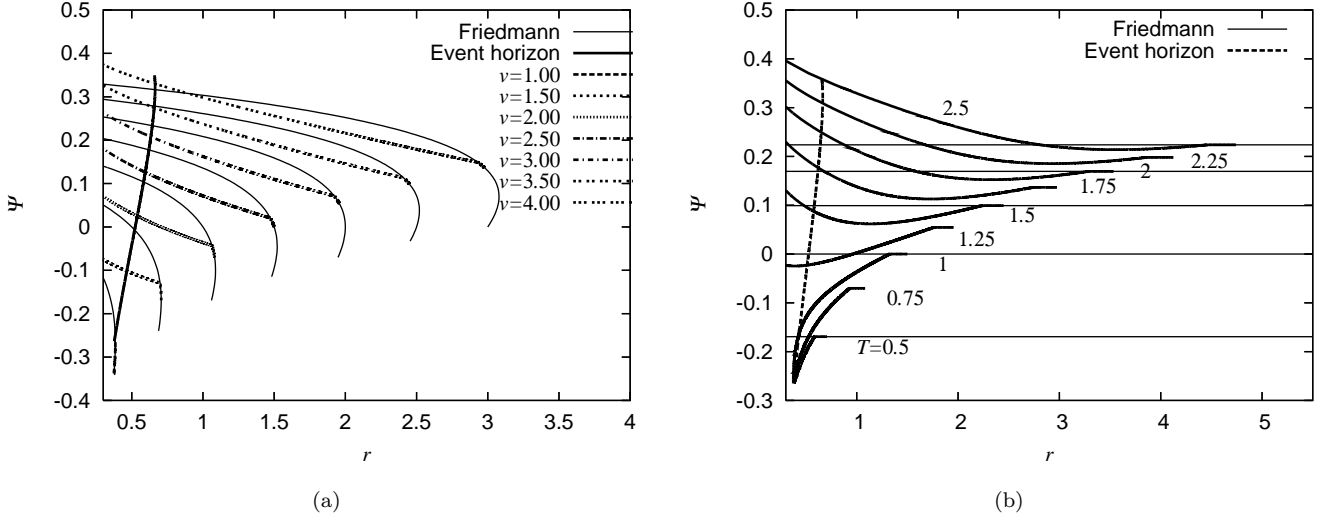


FIG. 10: The snapshots of scalar field profiles for Model A. In (a) the profiles are indicated by solid curves for the numerical simulations and by dashed curves for the flat Friedmann solution. In (b) they are indicated by heavy and light curves, respectively, and the broken line gives the position of the event horizon.

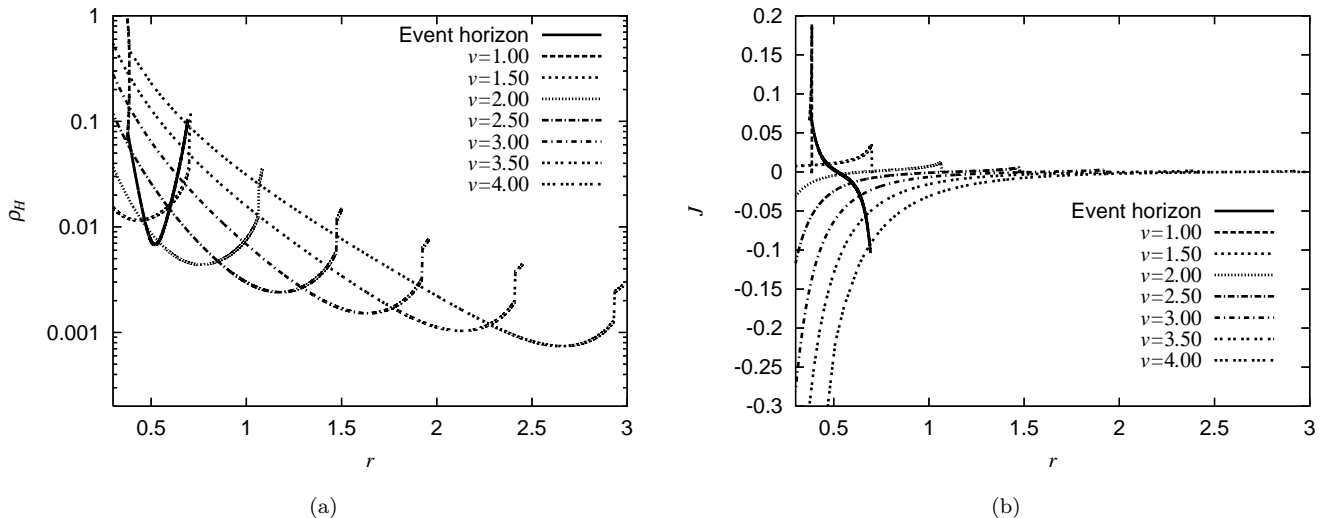


FIG. 11: The snapshots of the energy density ρ_H and the momentum density J of the scalar field measured by the observer moving normal to the $T = (u + v)/2 = \text{const}$ spacelike hypersurface for Model A.

quintessence field. It also provides a counterexample to the proposal that a spherically symmetric spacetime always evolves towards self-similarity [7].

B. Gravitational memory?

The Brans-Dicke theory with empty stress-energy tensor can be transformed into the Einstein theory with a massless scalar field by a conformal transformation even when the Brans-Dicke parameter ω is of order unity [17]. This is also the case in scalar-tensor theories of gravity if there is a single massless gravitational scalar field. The transformed frame with the Einstein-Hilbert action is called the Einstein frame, in contrast to the original physical frame. The gravitational constant varies in space and time in the physical frame and is actually a function of the massless scalar

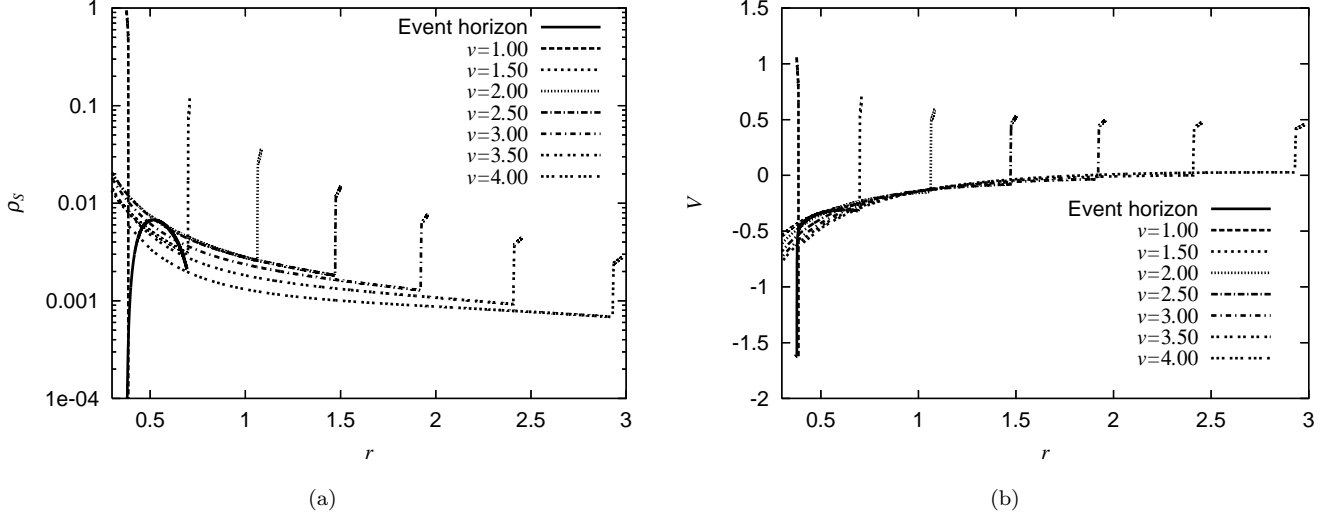


FIG. 12: The snapshots of (a) the energy density ρ_s and (b) the velocity V of the stiff fluid equivalent to the scalar field for Model A. It is noted that both ρ_s and V are observer-independent.

field Ψ in the Einstein frame. Since the conformal transformation does not affect the causal structure of the spacetime, the present simulation can be regarded as probing the evolution of PBHs in Brans-Dicke and scalar-tensor theories with empty stress-energy tensor.

Our results elucidate whether or not gravitational memory is physically reasonable [29]. We have seen that the scalar field evolution near and even inside the black hole event horizon follows the cosmological evolution. Moreover, the gradient of the scalar field is always timelike. Therefore, we conclude that the evolution of the physical gravitational constant near a PBH in Brans-Dicke and scalar-tensor theories essentially follows its asymptotic cosmological evolution. The fact that the gradient of the scalar field is timelike during the evolution also assures the existence of a spacetime foliation with spacelike hypersurfaces, in which the physical gravitational constant is spatially constant. Therefore, we conclude that the gravitational memory scenario is physically unrealistic even for PBHs whose size is comparable with the cosmological horizon.

Using a perturbative test field analysis, Jacobson [20] showed that black holes do not exhibit gravitational memory in scalar-tensor cosmology if they are much smaller than the cosmological horizon. Numerical studies for a test scalar field in the PBH dust solution by Harada, Goymer and Carr [21] showed that there is no gravitational memory even for black holes whose size is comparable to the cosmological horizon scale, so long as the back reaction of the scalar field on the metric can be neglected. In the present work we have extended this result by considering the case where the black hole size is comparable to the cosmological horizon scale and the gravitational effect of the scalar field is included. Once the black hole horizon gets much smaller than the cosmological horizon scale, the approximation made by Jacobson will apply. Taken together, these results suggest that the gravitational memory scenario is a highly unphysical, at least in Brans-Dicke and scalar-tensor theories.

VI. CONCLUSION

We have investigated the evolution of a PBH in a flat Friedmann universe with a massless scalar field by numerically integrating the Einstein field equations using the double-null formulation. We have considered models in which a Schwarzschild interior and a Friedmann exterior are matched at a finite radius with some smoothing length. For PBHs which are initially the same size as or smaller than the cosmological apparent horizon, the black hole event horizon soon becomes smaller than the cosmological horizon scale. The black hole apparent horizon forms inside the black hole event horizon but asymptotes towards it.

The scalar field evolution qualitatively follows the cosmological evolution close to the black hole event horizon and even inside it. The scalar field maintains a timelike gradient and is therefore always equivalent to a stiff fluid. In terms of the stiff fluid description, the energy density in the perturbed region decreases homogeneously in time and the infall velocity profile near the black hole becomes almost stationary after a short time.

Our results show that, soon after the PBH enters the cosmological apparent horizon, it becomes isolated from the cosmological expansion, with only a very small amount of mass accretion from the non-vacuum exterior. The accretion can be significant at first but soon decreases and becomes insignificant. In particular, our simulations exhibit no self-similar growth of the PBH. This is consistent with earlier work, which proved the non-existence of self-similar PBH solutions for a stiff fluid with an exact flat Friedmann exterior. The present result also indicates that the gravitational memory scenario for PBHs is unphysical in Brans-Dicke and scalar-tensor theories of gravity.

Acknowledgments

We would like to thank J. Miller and I. Musco for helpful discussion. TH was supported from JSPS.

APPENDIX A: BASIC EQUATIONS

We put

$$s = \sqrt{4\pi}\Psi. \quad (\text{A1})$$

From the Einstein equations and the equation of motion, we have the following partial differential equations:

$$A_{,u} = 2Ac, \quad (\text{A2})$$

$$A_{,v} = 2Ad, \quad (\text{A3})$$

$$r_{,u} = f, \quad (\text{A4})$$

$$r_{,v} = g, \quad (\text{A5})$$

$$s_{,u} = p, \quad (\text{A6})$$

$$s_{,v} = q, \quad (\text{A7})$$

$$p_{,v} = -\frac{\mu}{r}, \quad (\text{A8})$$

$$q_{,u} = -\frac{\mu}{r}, \quad (\text{A9})$$

$$c_{,v} = \frac{\lambda}{r^2} - pq, \quad (\text{A10})$$

$$d_{,u} = \frac{\lambda}{r^2} - pq, \quad (\text{A11})$$

$$f_{,v} = -\frac{\lambda}{r}, \quad (\text{A12})$$

$$g_{,u} = -\frac{\lambda}{r}, \quad (\text{A13})$$

$$f_{,u} = 2cf - rp^2, \quad (\text{A14})$$

$$g_{,v} = 2dg - rq^2, \quad (\text{A15})$$

where

$$\lambda = fg + \frac{1}{4}A, \quad (\text{A16})$$

$$\mu = fq + gp. \quad (\text{A17})$$

The physical quantities defined in the text can be expressed in terms of the quantities introduced above as follows:

$$m = \frac{r}{2} \left(1 + \frac{4fg}{A} \right), \quad (\text{A18})$$

$$\rho_H = \frac{p^2 + q^2}{8\pi A}, \quad (\text{A19})$$

$$J = \frac{q^2 - p^2}{8\pi A}, \quad (\text{A20})$$

$$\rho_S = \frac{pq}{4\pi A}, \quad (A21)$$

$$V = \frac{fq + gp}{\sqrt{2Apq}}. \quad (A22)$$

APPENDIX B: EXACT SOLUTIONS IN THE DOUBLE-NULL FORMULATION

1. Flat Friedmann solution

The flat Friedmann solution with a massless scalar field can be written as

$$ds^2 = A[-d\eta^2 + d\chi^2 + \chi^2(d\theta^2 + \sin^2\theta d\phi^2)], \quad (B1)$$

where $A = C^2\eta$ and C is a positive constant. This solution can be rewritten in double-null coordinates as

$$ds^2 = -Adudv + r^2(d\theta^2 + \sin^2\theta d\phi^2), \quad (B2)$$

$$A = C^2 \left(\frac{u+v}{2} \right), \quad (B3)$$

$$r = C \left(\frac{u+v}{2} \right)^{1/2} \left(\frac{v-u}{2} \right), \quad (B4)$$

$$s = \frac{\sqrt{3}}{2} \ln \left(\frac{u+v}{2} \right) + s_0, \quad (B5)$$

where s_0 is an arbitrary constant, and u and v are related to η and χ through

$$u = \eta - \chi, \quad v = \eta + \chi, \quad (B6)$$

respectively. The cosmological time t , where $dt = A^{1/2}d\eta$, t is given by

$$t = \frac{2}{3}C\eta^{3/2}. \quad (B7)$$

The Hubble parameter $H = d\ln\sqrt{A}/dt$ is given by

$$H = \frac{1}{2C} \left(\frac{u+v}{2} \right)^{-3/2}. \quad (B8)$$

There are two important horizons in this spacetime: the cosmological particle horizon and the cosmological apparent horizon. In the above coordinates, the cosmological particle horizon is given by $u = 0$ or $\eta = \chi$, while the cosmological apparent horizon is given by $3u + v = 0$ or $\eta = \chi/2$. Hence, the cosmological apparent horizon is spacelike and outside the cosmological particle horizon. The conformal diagram of the flat Friedmann solution is described in Fig. 1.

The physical quantities are

$$m = \frac{C}{16\sqrt{2}} \frac{(v-u)^3}{(v+u)^{3/2}}, \quad (B9)$$

$$\rho_H = \frac{3}{8\pi C^2} \frac{1}{(u+v)^3}, \quad (B10)$$

$$J = 0, \quad (B11)$$

$$\rho_S = \frac{3}{8\pi C^2} \frac{1}{(u+v)^3}, \quad (B12)$$

$$V = \frac{1}{2\sqrt{2}} \frac{v-u}{v+u}. \quad (B13)$$

This solution admits the following initial data:

$$s(u_0, v) = \frac{\sqrt{3}}{2} \ln \left(\frac{u_0+v}{2} \right) + s_0, \quad (B14)$$

$$s(u, v_0) = \frac{\sqrt{3}}{2} \ln \left(\frac{u + v_0}{2} \right) + s_0, \quad (\text{B15})$$

$$A(u_0, v) = C^2 \left(\frac{u_0 + v}{2} \right), \quad (\text{B16})$$

$$A(u, v_0) = C^2 \left(\frac{u + v_0}{2} \right), \quad (\text{B17})$$

and

$$r(u_0, v_0) = C \left(\frac{u_0 + v_0}{2} \right)^{1/2} \left(\frac{v_0 - u_0}{2} \right), \quad (\text{B18})$$

$$f(u_0, v_0) = r(u_0, v_0) \left[\frac{1}{2(u_0 + v_0)} - \frac{1}{v_0 - u_0} \right], \quad (\text{B19})$$

$$g(u_0, v_0) = r(u_0, v_0) \left[\frac{1}{2(u_0 + v_0)} + \frac{1}{v_0 - u_0} \right]. \quad (\text{B20})$$

2. Schwarzschild solution

The Schwarzschild solution is given by

$$ds^2 = - \left(1 - \frac{2M}{r} \right) dt^2 + \left(1 - \frac{2M}{r} \right)^{-1} dr^2 + r^2(d\theta^2 + \sin^2 \theta d\phi^2). \quad (\text{B21})$$

This can be rewritten in double-null coordinates as

$$ds^2 = - \left(1 - \frac{2M}{r} \right) dudv + r^2(d\theta^2 + \sin^2 \theta d\phi^2), \quad (\text{B22})$$

where u and v are given by

$$u = t - r_*, \quad v = t - r_*, \quad \frac{dr_*}{dr} = \left(1 - \frac{2M}{r} \right)^{-1}. \quad (\text{B23})$$

However, as is well known, this coordinate system cannot penetrate into the inside of the black hole event horizon. We therefore consider another coordinate system. For example, we can prescribe the initial data for this solution as follows:

$$A(u_0, v) = A(u, v_0) = \text{const}, \quad (\text{B24})$$

$$s(u_0, v) = s(u, v_0) = s_0, \quad (\text{B25})$$

$$r(u_0, v_0) = r_0, \quad (\text{B26})$$

$$f(u_0, v_0) = -\frac{1}{2}, \quad (\text{B27})$$

$$g(u_0, v_0) = \frac{A}{2} \left(1 - \frac{2M}{r_0} \right). \quad (\text{B28})$$

APPENDIX C: NUMERICAL CODE DETAILS

The basic equations are written in the form (A2)–(A17). Along the direction dv we use (A3), (A5), (A7), (A8), (A12), and (A15). Along the direction du we use (A9) and (A11). We do not use (A2), (A4), (A6), (A10), (A13), and (A14) except for determining boundary values and error estimates. For physical variables, we calculate A , r , s , d , f , g , p and q . We do not calculate c . Numerical accuracy is monitored by the relative errors in Eqs. (A4), (A6) and (A13).

We use the two-step finite differencing scheme proposed by Hamadé and Stewart [22]. First we write the equations schematically as

$$y_{,u} = F(y, z), \quad (\text{C1})$$

$$z_{,v} = G(y, z), \quad (\text{C2})$$

where in this special case,

$$y = \begin{pmatrix} q \\ d \end{pmatrix}, \quad F = \begin{pmatrix} -\frac{\mu}{r} \\ \frac{\lambda}{r^2} + pq \end{pmatrix}, \quad (C3)$$

$$z = \begin{pmatrix} A \\ r \\ s \\ g \\ f \\ p \end{pmatrix}, \quad G = \begin{pmatrix} 2Ad \\ g \\ q \\ 2dg - rq^2 \\ -\frac{\lambda}{r} \\ -\frac{\mu}{r} \end{pmatrix}. \quad (C4)$$

At the first step we predict the values at $n(u, v)$ using those at $w(u, v - h)$ and $e(u - h, v)$ as

$$\hat{y}_n = y_e + hF(y_e, z_e), \quad (C5)$$

$$\hat{z}_n = z_w + \frac{1}{2}h(G(y_w, z_w) + G(\hat{y}_n, \hat{z}_n)). \quad (C6)$$

At the second step we correct the prediction via

$$y_n = \frac{1}{2}(\hat{y}_n + y_e + hF(\hat{y}_n, \hat{z}_n)), \quad (C7)$$

$$z_n = \frac{1}{2}(\hat{z}_n + z_w + hG(\hat{y}_n, \hat{z}_n)). \quad (C8)$$

Due to Eq. (C8), however, the scheme is only accurate to first-order. If instead we use

$$z_n = \hat{z}_n, \quad (C9)$$

then the scheme is accurate to second-order. We have used the latter scheme because it does not suffer from numerical instability for the calculated models.

In general, Eq. (C6) can be implemented only implicitly. However, in this special case, it is possible to determine \hat{z}_n explicitly as follows:

$$\hat{s}_n = \tilde{s}_w + \frac{1}{2}h\hat{q}_n, \quad (C10)$$

$$\hat{A}_n = \frac{\tilde{A}_w}{1 - h\hat{d}_n}, \quad (C11)$$

$$\begin{pmatrix} \hat{r}_n \\ \hat{g}_n \end{pmatrix} = \frac{1}{1 - h\hat{d}_n + \frac{1}{4}h^2\hat{q}_n^2} \begin{pmatrix} 1 - h\hat{d}_n & \frac{1}{2}h \\ -\frac{1}{2}h\hat{q}_n^2 & 1 \end{pmatrix} \begin{pmatrix} \tilde{r}_w \\ \tilde{g}_w \end{pmatrix}, \quad (C12)$$

$$\hat{f}_n = \frac{\tilde{f}_w - \frac{1}{8}h\frac{\hat{A}_n}{\hat{r}_n}}{1 + \frac{1}{2}h\frac{\hat{g}_n}{\hat{r}_n}}, \quad (C13)$$

$$\hat{p}_n = \frac{\tilde{p}_w - \frac{1}{2}h\frac{\hat{f}_n\hat{q}_n}{\hat{r}_n}}{1 + \frac{1}{2}h\frac{\hat{g}_n}{\hat{r}_n}}, \quad (C14)$$

where we put

$$\tilde{z}_w \equiv z_w + \frac{1}{2}hG(y_w, z_w). \quad (C15)$$

Note that the order of determination is very important here.

- [1] S. W. Hawking, Mon. Not. R. Astron. Soc. **152**, 75 (1971).
- [2] B. J. Carr, Astrophys. J. **201**, 1 (1975).
- [3] B. J. Carr and S. W. Hawking, Mon. Not. R. Astron. Soc. **168**, 339 (1974).
- [4] D. N. C. Lin, B. J. Carr and S. M. Fall, Mon. Not. R. Astron. Soc. **177**, 51 (1976).
- [5] G. V. Bicknell and R. N. Henriksen, Astrophys. J. **219**, 1043 (1978).
- [6] G. V. Bicknell and R. N. Henriksen, Astrophys. J. **225**, 237 (1978).
- [7] B. J. Carr and A. A. Coley, Class. Quantum Grav. **17**, 4339 (2000).
- [8] D. K. Nadezhin, I. D. Novikov and A. G. Polnarev, Sov. Astron. **22**, 129, (1978).
- [9] I. D. Novikov and A. G. Polnarev, Sov. Astron. **24**, 147, (1980).
- [10] J. C. Niemeyer and K. Jedamzik, Phys. Rev. D **59**, 124013 (1999).
- [11] K. Jedamzik and J. C. Niemeyer, Phys. Rev. D **59**, 124014 (1999).
- [12] M. Shibata and M. Sasaki, Phys. Rev. D **60**, 084002 (1999).
- [13] J. Miller, I. Musco and L. Rezzola, in preparation.
- [14] L. Kofman, A. Linde, and A. A. Starobinsky, Phys. Rev. Lett. **73**, 3195 (1994); Phys. Rev. D **56**, 3258 (1997)
- [15] R. Bean and J. Magueijo, Phys. Rev. D **66**, 063505 (2002).
- [16] A. V. Frolov, preprint, SU-ITP-04-13, SLAC-PUB-10473, hep-th/0404216.
- [17] T. Damour and G. Esposito-Farese, Class. Quantum Grav. **9**, 2093 (1992).
- [18] J. D. Barrow, Phys. Rev. D **46**, R3227 (1992).
- [19] J. D. Barrow and B. J. Carr, Phys. Rev. D **54**, 3920 (1996).
- [20] T. Jacobson, Phys. Rev. Lett. **83**, 2699 (1999).
- [21] T. Harada, C. Goymer and B. J. Carr, Phys. Rev. D **66**, 104023 (2002).
- [22] R. S. Hamadé and J. M. Stewart, Class. Quantum Grav. **13**, 497 (1996).
- [23] E. Sorkin and T. Piran, Phys. Rev. D **63**, 084006 (2001).
- [24] T. Harada and B. J. Carr, in preparation (2004a).
- [25] T. Harada and B. J. Carr, in preparation (2004b).
- [26] R. M. Wald, *General Relativity*, (University of Chicago Press, Chicago, 1983).
- [27] M. S. Madsen, Class. Quantum Grav. **5**, 627 (1988).
- [28] S. W. Hawking, Phys. Rev. Lett. **26**, 1344 (1971).
- [29] B. J. Carr and C. A. Goymer, Prog. Theor. Phys. **136**, 321 (1999).